

Article

# Internal Vibrations of Pyridinium Cation in One-Dimensional Halide Perovskites and the Corresponding Halide Salts

Anna Yu. Samsonova <sup>1,\*</sup>, Alena Yu. Mikheleva <sup>1</sup>, Kirill M. Bulanin <sup>1</sup>, Nikita I. Selivanov <sup>1</sup>, Anton S. Mazur <sup>2</sup>, Peter M. Tolstoy <sup>3</sup> , Constantinos C. Stoumpos <sup>1,4,\*</sup> and Yury V. Kapitonov <sup>1</sup>

<sup>1</sup> Photonics of Crystals Laboratory, Saint Petersburg State University, Ulyanovskaya d.1, 198504 St. Petersburg, Russia

<sup>2</sup> Magnetic Resonance Research Center, Saint Petersburg State University, Universitetskiy pr. 26, 198504 St. Petersburg, Russia; a.mazur@spbu.ru

<sup>3</sup> Institute of Chemistry, Saint Petersburg State University, Universitetskiy pr. 26, 198504 St. Petersburg, Russia

<sup>4</sup> Department of Materials Science and Technology, University of Crete, Voutes, GR-70013 Heraklion, Greece

\* Correspondence: a.y.samsonova@spbu.ru (A.Y.S.); cstoumpos@materials.uoc.gr (C.C.S.)

**Abstract:** We investigate vibrations of the pyridinium cation  $\text{PyH}^+ = \text{C}_5\text{H}_5\text{NH}^+$  in one-dimensional lead halide perovskites  $\text{PyPbX}_3$  and pyridinium halide salts  $\text{PyHX}$  ( $\text{X}^- = \text{I}^-, \text{Br}^-$ ), combining infrared absorption and Raman scattering methods at room temperature. Internal vibrations of the cation were assigned based on density functional theory modeling. Some of the vibrational bands are sensitive to perovskite or the salt environment in the solid state, while halide substitution has only a minor effect on them. These findings have been confirmed by  $^1\text{H}$ ,  $^{13}\text{C}$  and  $^{207}\text{Pb}$  solid-state nuclear magnetic resonance (NMR) experiments. Narrower vibrational bands in perovskites indicate less disorder in these materials. The splitting of NH-group vibrational bands in perovskites can be rationalized the presence of nonequivalent crystal sites for cations or by more exotic phenomena such as quantum tunneling transition between two molecular orientations. We have shown how organic cations in hybrid organic–inorganic crystals could be used as spectators of the crystalline environment that affects their internal vibrations.

**Keywords:** halide perovskites; Raman scattering; IR absorption; solid-state NMR; molecular vibrations



**Citation:** Samsonova, A.Y.;

Mikheleva, A.Y.; Bulanin, K.M.;

Selivanov, N.I.; Mazur, A.S.; Tolstoy,

P.M.; Stoumpos, C.C.; Kapitonov, Y.V.

Internal Vibrations of Pyridinium Cation in One-Dimensional Halide Perovskites and the Corresponding Halide Salts. *Molecules* **2024**, *29*, 78.

[https://doi.org/10.3390/](https://doi.org/10.3390/molecules29010078)

[molecules29010078](https://doi.org/10.3390/molecules29010078)

Academic Editor: Marco Anni

Received: 1 December 2023

Revised: 19 December 2023

Accepted: 20 December 2023

Published: 22 December 2023



**Copyright:** © 2023 by the authors. Licensee MDPI, Basel, Switzerland. This article is an open access article distributed under the terms and conditions of the Creative Commons Attribution (CC BY) license (<https://creativecommons.org/licenses/by/4.0/>).

## 1. Introduction

The last decade has witnessed an increase in the interest in hybrid organic–inorganic lead-based halide perovskites due to their optoelectronic and photovoltaic applications [1–4]. This family of materials is valuable due to the wide variety of crystal structures, the most studied and used of which are three-dimensional (3D) lead halide perovskites with the chemical formula  $\text{APbX}_3$  ( $\text{X}^- = \text{I}^-, \text{Br}^-, \text{Cl}^-$ ). The 3D crystal framework is formed by the corner-shared lead-halide octahedra and small organic cations  $\text{A}^+$  between them ( $\text{A}^+ = \text{CH}_3\text{NH}_3^+ = \text{MA}^+$ ,  $\text{HC}(\text{NH}_2)^+ = \text{FA}^+$ ). Substitution of the organic cation  $\text{A}^+$  by a larger cation leads to the formation of low-dimensional perovskite-like structures, consisting of two-dimensional (2D) sheets [5,6] or one-dimensional (1D) chains [7,8] of lead-halide octahedra and the organic cations filling the space between them. Further, for brevity, such structures are designated as low-dimensional perovskites.

The movement of organic cations in hybrid lead halide perovskites and their low-dimensional analogues is the key to understanding the features of the crystal structure and its phase transitions. In case of 3D hybrid lead halide perovskites, order–disorder changes in the methylammonium ( $\text{MA}^+$ ) and formamidinium ( $\text{FA}^+$ ) cations were shown to be responsible for the distortion of the lead halide inorganic framework leading to the dynamic disorder at high temperatures [9–13].  $\text{MA}^+$  and  $\text{FA}^+$  cations behave similarly in the high-temperature and intermediate-temperature phases, rotating isotropically and reorienting between their preferred orientations, respectively [9,14–19]. In the low-temperature phase,

MA<sup>+</sup> cations still have an ordered three-fold rotational axis [17,20], while the FA<sup>+</sup> cations are locally disordered, exhibiting a glass-like state in the arrangement of the cations [14]. In 2D perovskites, large organic cations have greater freedom of motion compared to 3D perovskites and tend to interact with each other by weak intermolecular forces and with the inorganic framework through strong electrostatic interactions [5,6,21–23]. In addition, the motion of organic cations in these materials is responsible for order–disorder structural phase transitions with their symmetry breaking due to the concerted alignment of organic cations across a specific dipole moment vector direction [24–26]. For 1D hybrid halide perovskites, a major group of which are perovskites with face-shared octahedra assembled into the inorganic chains, organic cations are found to demonstrate behavior similar to that in their 2D counterparts [27–30].

To study the organic subsystem of hybrid halide perovskites, neutron [9] and X-ray diffraction (XRD) [9,10,24–32], solid-state nuclear magnetic resonance (NMR), quasielastic neutron scattering (QENS) [14–17], Raman [10–13,21–24,33] scattering methods and density functional theory (DFT) modeling [22,31,34] are widely used. The vibrational properties of inorganic perovskite frameworks have been studied in the literature [5,10,21,23]. Insufficient attention has been paid to the use of such relatively experimentally convenient methods as infrared (IR) and Raman spectroscopy for the study vibrations of the organic subsystem in perovskites. Organic cations are spectators of the crystalline environment [22,35]. The polarized Raman spectroscopy of organic vibrations could be used to determine the crystal orientation [33] and the cation movement [20].

Of particular interest is the movement of the simple aromatic pyridinium cation PyH<sup>+</sup> = C<sub>5</sub>H<sub>5</sub>NH<sup>+</sup>, which stabilizes both perovskite-like compounds and PyHX (X<sup>−</sup> = I<sup>−</sup>, Br<sup>−</sup>) salts [36–40]. The hybrid halide perovskites PyPbX<sub>3</sub> (X<sup>−</sup> = I<sup>−</sup>, Br<sup>−</sup>) have the 1D structure of face-shared octahedra chains [31,32,41,42].

In this work, we studied the vibrational properties of the pyridinium cation in hybrid halide perovskites PyPbX<sub>3</sub> (X<sup>−</sup> = I<sup>−</sup>, Br<sup>−</sup>). IR and Raman spectra of these perovskites are compared with ones for PyHX (X<sup>−</sup> = I<sup>−</sup>, Br<sup>−</sup>) salts. Based on theoretical modeling, we identified the observed vibrations. Frequencies were identified that were most sensitive to changing the crystalline environment of the PyH<sup>+</sup> cation from salt to perovskite, while replacing halogen usually had less effect. The latter statement is also confirmed by the solid-state NMR examination of organic cations. We also address the possible origins of the splitting of several bands involving cation NH-vibrations in perovskites.

## 2. Results and Discussion

### 2.1. Synthesis and Crystal Structure

Pyridinium lead trihalide PyPbX<sub>3</sub> (X<sup>−</sup> = I<sup>−</sup>, Br<sup>−</sup>) single crystals (see photos of the samples on Figure S1) were grown by the slow counterdiffusion of ions from individual solutions of lead(II) halides and pyridine in hydrohalic acid in the silica gel filled U-tube. Pyridine hydrohalides PyHX (X<sup>−</sup> = I<sup>−</sup>, Br<sup>−</sup>) were synthesized by adding concentrated hydrogen halogenides drop-wise with constant stirring to the solutions of ethanol and pyridine. More details on the synthesis can be found in the Methods section (Section 3).

The typical crystal structure of PyHX salts (X<sup>−</sup> = I<sup>−</sup>, Br<sup>−</sup>) is shown in Figure 1a [43]. Upon heating from cryogenic to room temperature, these materials undergo an order–disorder phase transition from the monoclinic to the rhombohedral phase, in which the previously frozen PyH<sup>+</sup> cations begin to rotate around the pseudo-six-fold axis (“C<sub>6</sub>”) (Figure 1c) [37–39]. The order–disorder phase transitions and molecular motions of the PyH<sup>+</sup> cation in various compounds have been studied [36–40,44–47]. Pyridinium internal vibrational modes are shown to be sensitive to such phase transitions [48–51].

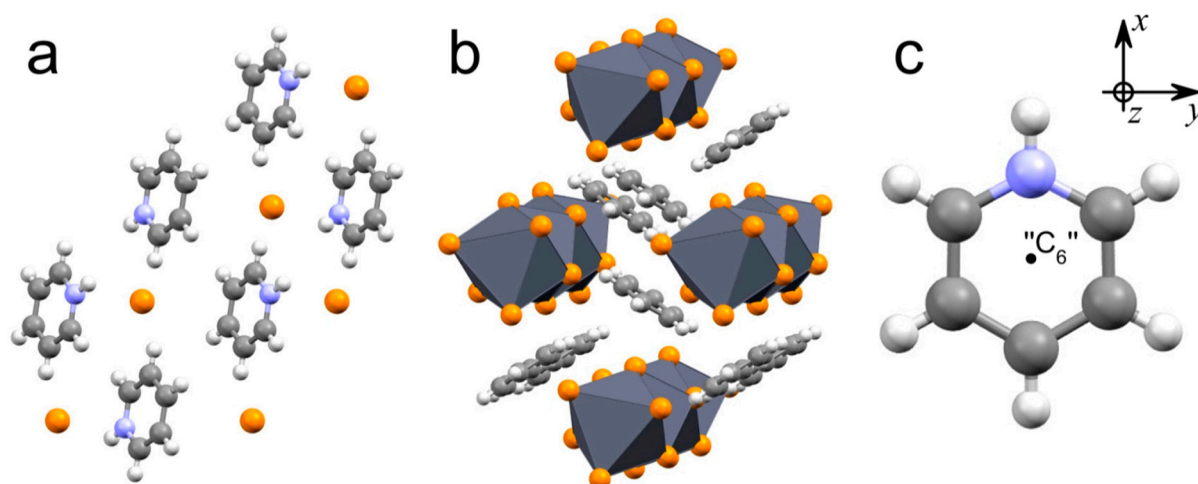


**Figure 1.** Typical crystal structure of PyHX [43,52] (a) and PyPbX<sub>3</sub> [31,32,41,42] ( $X^- = I^-, Br^-$ ) (b). (c) PyH<sup>+</sup> cation. Gray—carbon atoms; blue—nitrogen atoms; white—hydrogen atoms; orange—halide atoms; dark grey—PbX<sub>6</sub> octahedra.

The crystal structure of PyPbX<sub>3</sub> ( $X^- = I^-, Br^-$ ) perovskites consists of 1D chains of face-shared lead halide octahedra and tightly packed PyH<sup>+</sup> cations between them (Figure 1b) [31,32,41,42]. At room temperature, the compounds crystallize in the orthorhombic space group *Pnma* with each unit cell containing two chains running down the crystallographic *b*-axis and isolated from one another by individual PyH<sup>+</sup> cations [32]. In the case of the simple salts, pyridinium cations can be found in a totally disordered state (PyHI, 293 K) [43] or a totally ordered state (PyHBr, 100 K) [52] depending on whether the intermolecular forces are strong enough to dominate over the thermal motion.

In both cases, the pyridinium cations remain essentially isolated from their surroundings. Thus, to analyze their internal vibrations, we will consider the vibrations of free cations as a first approximation and then estimate the influence of the crystalline environment on them. Another possible approach is to calculate the vibrations of cations in clusters, which are fragments of the crystal lattice [34].

## 2.2. Symmetry Considerations

To identify vibrations of pyridinium cations, we first consider the benzene (C<sub>6</sub>H<sub>6</sub>) molecule. We would like to note that the assignment of vibrational modes in the spectra of these molecules is a subject of discussion in the literature. To denote the vibrational modes of the PyH<sup>+</sup> cation, we follow the Wilson notation [53], which was introduced to denote vibrational modes of the benzene C<sub>6</sub>H<sub>6</sub> molecule and has been commonly used for the vibrational modes assignment of C<sub>6</sub>H<sub>6</sub> derivatives [49,51,54].

The benzene C<sub>6</sub>H<sub>6</sub> molecule belongs to the D<sub>6h</sub> point group and contains a main C<sub>6</sub> axis which contains S<sub>6</sub> and S<sub>3</sub> axes. Three C<sub>2</sub> and three C<sub>2'</sub> axes are perpendicular to the C<sub>6</sub> axis and are passing through the middle of the bonds between carbon atoms and carbon atoms themselves, respectively. There are one σ<sub>h</sub>, three σ<sub>v</sub> and three σ<sub>d</sub> planes, an inversion center, as well as twelve irreducible representations (see the character table in Table S1).

The PyH<sup>+</sup> cation (Figure 1c) can be considered as a C<sub>6</sub>H<sub>6</sub> molecule in which one of the carbon atoms is replaced by a nitrogen atom. It leads to the loss of benzene symmetry operations except for the reflection in the one vertical plane σ<sub>v</sub>, rotation around the C<sub>2'</sub> axis lying in the σ<sub>v</sub> plane and reflection in the horizontal plane σ<sub>h</sub> (Figure S2). These symmetry operations form the C<sub>2v</sub> point group (see the character table in Table S2) and should be renamed as C<sub>2'</sub> → C<sub>2</sub>, σ<sub>h</sub> → σ<sub>d</sub> and σ<sub>v</sub> → σ<sub>v</sub>. The twelve irreducible representations of the D<sub>6h</sub> point group are reduced to the four irreducible representations of the C<sub>2v</sub> point group (Table S3), which are A<sub>1</sub>, A<sub>2</sub>, B<sub>1</sub>, B<sub>2</sub>. Here, we align the C<sub>2</sub> axis with the *x*-axis in the Cartesian coordinate system. Indexes 1 and 2 denote the symmetry and asymmetry

with respect to the reflection in the  $\sigma_v$  plane. Indexes A and B denote the symmetry and asymmetry with respect to the rotation around the  $C_2$  axis.

The  $C_6H_6$  molecule and  $PyH^+$  cation both have  $N = 12$  atoms and  $3N = 36$  degrees of freedom. In the case of an isolated cation or molecule, only the change in the position of the atoms relative to each other matters. Therefore, 36 degrees of freedom can be reduced by 6, of which 3 are translational movements and 3 are rotational movements of the molecule or cation as a whole. This results in  $3N - 6 = 30$  internal vibrational modes of an isolated  $C_6H_6$  molecule or  $PyH^+$  cation. These modes are generated by one of the irreducible representations of the corresponding point symmetry group. The  $C_6H_6$  molecule has doubly degenerate normal modes. For the  $PyH^+$  cation, this degeneracy is removed and resulting modes are denoted by indexes *a* or *b*. This notation was introduced by Wilson [53] and is widely used [54,55].

### 2.3. DFT Modeling

IR and Raman wavenumbers and intensities of internal vibrational modes of the single  $C_6H_6$  molecule and  $PyH^+$  cation were calculated using DFT modeling (see Table 1). We use  $C_6H_6$  modes notations recently refined by Gardner et al. [55] based on Wilson's original work [53]. Correlating the vibrations of pyridinium with the established Wilson nomenclature for benzene requires care. We have assigned Wilson notation to pyridinium vibrational modes based on the correspondence between irreducible representations of the  $C_6H_6$  molecule and  $PyH^+$  cation (Table S3), calculated IR and Raman intensities for both molecules (Table 1) and the motions of atoms (Figure S3). Closely lying vibrations with the same symmetries could interact and mix upon transition from benzene to pyridinium. We denote such modes with a dash. In the strict sense, these modes could not be considered as pure Wilson modes, but they are combinations of them. It also could be seen from the comparison of atomic motions in Figure S3 and in Wilson modes [53,55].

**Table 1.** Calculated internal vibrational modes of  $C_6H_6$  molecule and  $PyH^+$  cation, and experimental bands for pyridinium salts and perovskites.

Benzene $C_6H_6$ (Calculated)				Pyridinium $PyH^+$ (Calculated)				Experiment, Freq., $cm^{-1}$ (IR,R)					
Sym.	Freq., $cm^{-1}$	$I_{thIR}$ , arb.u.	$I_{thR}$ , arb.u.	Sym.	Freq., $cm^{-1}$	$I_{thIR}$ , arb.u.	$I_{thR}$ , arb.u.	PyHI	PyHBr	PyPbI <sub>3</sub>	PyPbBr <sub>3</sub>		
$\nu_{16}$	$E_{2u}$	410.06	0.0	$\nu_{16b}$	$B_1$	389.19	0.851	0.269	390 (-,w)	399 (-,w)	380 (-,s)	379 (-,w)	
				$\nu_{16a}$	$A_2$	401.53	0.0	0.001	(-,0)	(-,0)	(-,0)	(-,0)	
$\nu_6$	$E_{2g}$	622.21	0.0	4.718	$\nu_{6a}$	$A_1$	622.88	0.014	2.883	607 (-,s)	607 (-,s)	607 (-,s)	608 (-,s)
					$\nu_{6b}$	$B_2$	646.15	0.398	5.125	633 (-,s)	635 (-,s)	635 (-,s)	634 (-,s)
$\nu_{11}$	$A_{2u}$	686.61	725.940	0.0	$\nu_{11'}$	$B_1$	674.76	92.175	0.019	681 (-,w)	685 (-,w)	657 (-,w)	662 (-,w)
$\nu_4$	$B_{2g}$	718.77	0.0	0.001	$\nu_4'$	$B_1$	743.62	88.368 *	0.022	753 (-,w)	757 (-,w)	726 (-,w)	727 (-,w)
$\nu_{10}$	$E_{1g}$	862.47	0.0	0.977	$\nu_{10b'}$	$B_1$	855.74	6.213 *	0.119	887 (-,s)	891 (-,w)	(-,0)	835 (-,w)
					$\nu_{10a}$	$A_2$	882.32	0.0	0.005	(-,0)	(-,0)	(-,0)	(-,0)
$\nu_{17}$	$E_{2u}$	987.00	0.0	0.0	$\nu_{17b'}$	$B_1$	989.76	1.795	0.049	993 (s,0)	993 (s,0)	968 (s,0)	971 (s,0)
					$\nu_{17a}$	$A_2$	1008.38	0.0	0.031	(0,0)	(0,0)	(0,0)	(0,0)

Table 1. Cont.

Benzene C <sub>6</sub> H <sub>6</sub> (Calculated)					Pyridinium PyH <sup>+</sup> (Calculated)					Experiment, Freq., cm <sup>-1</sup> (IR,R)			
	Sym.	Freq., cm <sup>-1</sup>	I <sub>th</sub> IR, arb.u.	I <sub>th</sub> R, arb.u.		Sym.	Freq., cm <sup>-1</sup>	I <sub>th</sub> IR, arb.u.	I <sub>th</sub> R, arb.u.	PyHI	PyHBr	PyPbI <sub>3</sub>	PyPbBr <sub>3</sub>
$\nu_1$	A <sub>1g</sub>	1011.61	0.0	98.763	$\nu_1$	A <sub>1</sub>	1018.61	3.442 *	52.390	1007 (s,s)	1008 (s,s)	1008 (s,s)	1008 (s,s)
$\nu_5$	B <sub>2g</sub>	1016.96	0.0	0.0	$\nu_5'$	B <sub>1</sub>	1046.99	0.573	0.0	(0,0)	(0,0)	(0,0)	1016 (m,0)
$\nu_{12}$	B <sub>1u</sub>	1022.46	0.0	0.0	$\nu_{12}$	A <sub>1</sub>	1048.31	1.280	10.132 *	1027 (s,s)	1028 (s,s)	1025 (s,s)	1026 (s,s)
$\nu_{19}$	E <sub>1u</sub>	1059.14	24.137	0.0	$\nu_{19a}$	A <sub>1</sub>	1078.43	3.178	1.006	1052 (s,s)	1054 (s,s)	1058 (s,m)	1058 (s,m)
					$\nu_{19b}$	B <sub>2</sub>	1081.89	5.159	0.317			1041 (s,m)	1046 (s,m)
$\nu_{14}$	B <sub>2u</sub>	1174.67	0.0	0.0	$\nu_{14}$	B <sub>2</sub>	1198.20	3.550	0.913	1150 (s,s)	1151 (s,s)	1156 (s,s)	1158 (s,s)
$\nu_8$	E <sub>2g</sub>	1197.33	0.0	5.225	$\nu_{8a}$	A <sub>1</sub>	1225.74	2.207	5.432	1186 (s,s)	1188 (s,s)	1188 (s,s)	1189 (s,s)
										1236 (s,s)	1238 (s,s)	1240 (s,s)	1252 (w,s)
					$\nu_{8b}$	B <sub>2</sub>	1290.23	4.616	3.836	1245 (s,s)	1247 (s,s)	1248 (s,s)	1258 (w,s)
										1327 (s,w)	1330 (s,w)	1323 (s,w)	1324 (s,w)
$\nu_{15}$	B <sub>2u</sub>	1337.39	0.0	0.0	$\nu_{15}$	B <sub>2</sub>	1359.06	10.665 *	0.483	1364 (s,w)	1367 (s,w)	1371 (s,0)	1375 (s,0)
$\nu_3$	A <sub>2g</sub>	1380.96	0.0	0.0	$\nu_3$	B <sub>2</sub>	1414.57	3.511	0.166	1478 (s,w)	1480 (s,w)	1478 (s,0)	1479 (s,w)
$\nu_{18}$	E <sub>1u</sub>	1510.48	18.87	0.0	$\nu_{18a}$	A <sub>1</sub>	1516.10	21.546	0.322	1526 (s,w)	1527 (s,0)	1482 (s,w)	1482 (s,w)
												1527 (s,0)	1529 (s,s)
					$\nu_{18b}$	B <sub>2</sub>	1573.78	39.154	0.135	1532 (s,0)	1536 (s,s)		
										1602 (s,s)	1600 (s,s)	1600 (s,s)	1603 (s,s)
$\nu_9$	E <sub>2g</sub>	1634.35	0.0	12.694	$\nu_{9a}$	A <sub>1</sub>	1664.58	34.814 *	15.265	1629 (s,s)	1632 (s,s)	1632 (s,w)	1633 (s,s)
$\nu_{13}$	B <sub>1u</sub>	3156.58	0.0	0.0	$\nu_{13'}$	A <sub>1</sub>	3201.51	0.254	60.939 *	?	?	?	?
					$\nu_{7b'}$	B <sub>2</sub>	3217.55	0.758	79.950	?	?	?	?
					$\nu_{7a'}$	A <sub>1</sub>	3550.84	163.241 *	77.094	2934 ** (s,?)	2818 ** (s,?)	3102 ** (s,?)	3064 ** (s,?)
$\nu_{20}$	E <sub>1u</sub>	3181.82	47.147	0.0	$\nu_{20a'}$	A <sub>1</sub>	3219.39	11.864	33.911 *	?	?	?	?
					$\nu_{20b'}$	B <sub>2</sub>	3229.71	21.724	10.687 *	?	?	?	?
$\nu_2$	A <sub>1g</sub>	3192.01	0.0	421.879	$\nu_2'$	A <sub>1</sub>	3231.40	0.273	240.672	3075 (?s)	3084 (?s)	3087 (?s)	3096 (?s)

The table is sorted by calculated frequencies of benzene. Symbols: '—mixed modes; \*—modes with substantial growth in activity in PyH<sup>+</sup> in comparison with C<sub>6</sub>H<sub>6</sub>; \*\*—modes position calculated as center-of-mass of the broad band; s—strong band; w—weak band; 0—vibration is not observed in the experiment; —no data for this region; ?—unable to determine frequency.

For some  $\text{PyH}^+$  cation vibrational modes, a substantial growth in activity is observed compared to those for the  $\text{C}_6\text{H}_6$  molecule. Such modes are marked with an asterisk in Table 1. However, in several cases, the  $\text{PyH}^+$  cation mode inherits the activity of a vibrational mode of the  $\text{C}_6\text{H}_6$  molecule, which was used as an additional criterion for mode designation. Next, the calculated pyridinium modes were correlated with the experimentally obtained ones.

#### 2.4. Vibrational Spectra Summary

The experimental IR and Raman spectra were measured for  $\text{PyHX}$  salts and  $\text{PyPbX}_3$  perovskites ( $\text{X}^- = \text{I}^-, \text{Br}^-$ ) at room temperature (Figures 2–4). The description of IR and Raman experiments could be found in the Methods section (Section 3). In this work, we focus on internal vibrations of the  $\text{PyH}^+$  cation lying above  $350\text{ cm}^{-1}$ . We will discuss three spectral regions: the low-frequency region  $80\text{--}930\text{ cm}^{-1}$  (Figure 3, only Raman), medium-frequency region  $930\text{--}1700\text{ cm}^{-1}$  with fingerprint vibrations (Figure 2, both IR and Raman) and high-frequency region of hydrogen modes  $1700\text{--}3600\text{ cm}^{-1}$  (Figure 4, both IR and Raman). Correlating calculated cation vibrations with observed bands is a rather difficult task, but simultaneous analysis of IR and Raman spectra in four different materials makes this correlation more reliable. Below, we will consider in more detail the various spectral regions and give reasons for the chosen correlation presented in Table 1. Here, we adopted the notation of  $\nu_8, \nu_9, \nu_{14}, \nu_{15}, \nu_{18}$  and  $\nu_{19}$  modes of benzene from Gardner et al.'s work [55]. Notation in other works may differ [51,54].

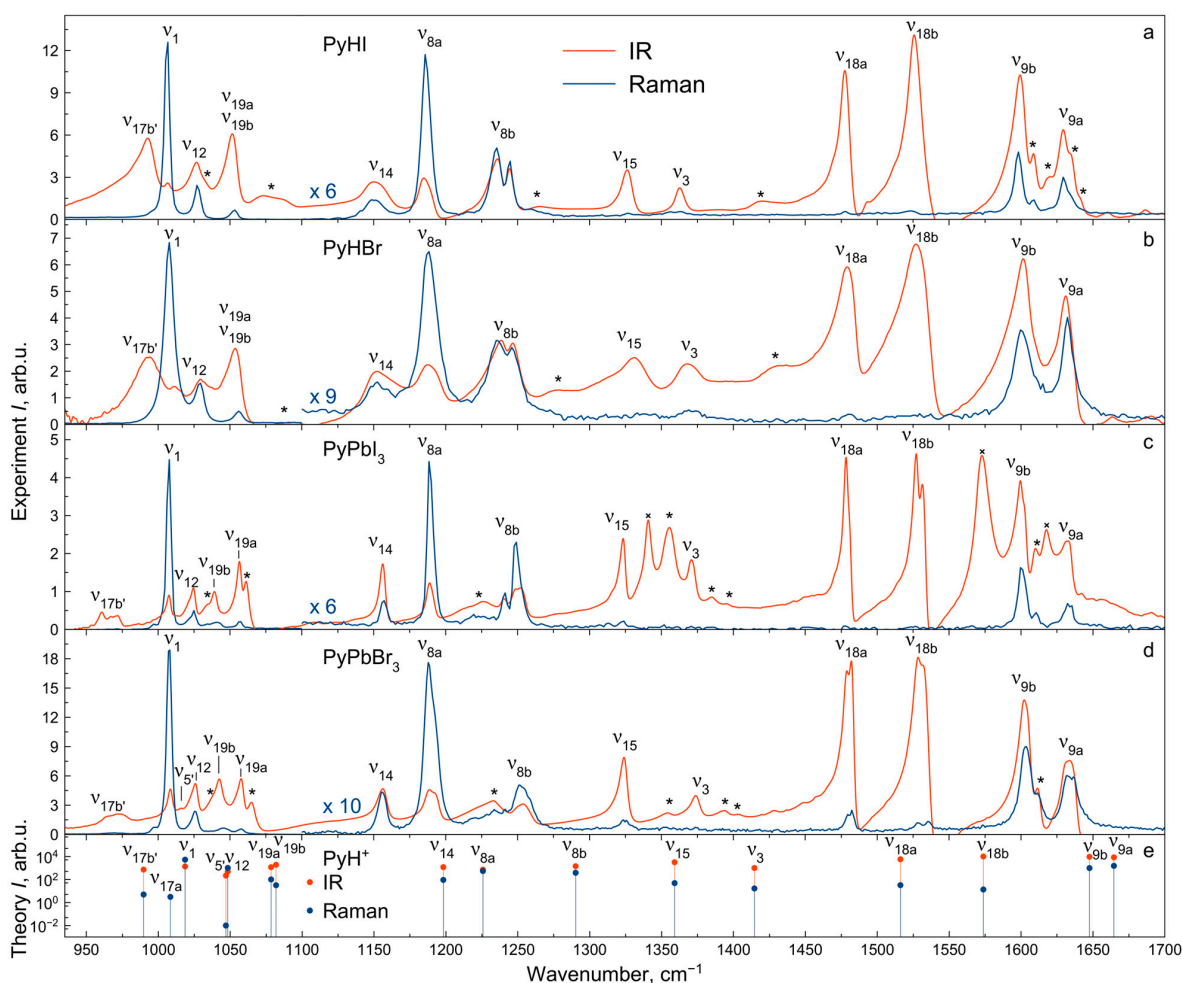


**Figure 2.** IR and Raman spectra of  $\text{PyHX}$  salts (a,b) and  $\text{PyPbX}_3$  perovskites ( $\text{X}^- = \text{I}^-, \text{Br}^-$ ) (c,d) at  $T = 300\text{ K}$ ; \*—combination modes; ×—KI contamination bands (observed also in KI powder). (e) Calculated IR (red) and Raman (blue) intensities of  $\text{PyH}^+$  cation modes.

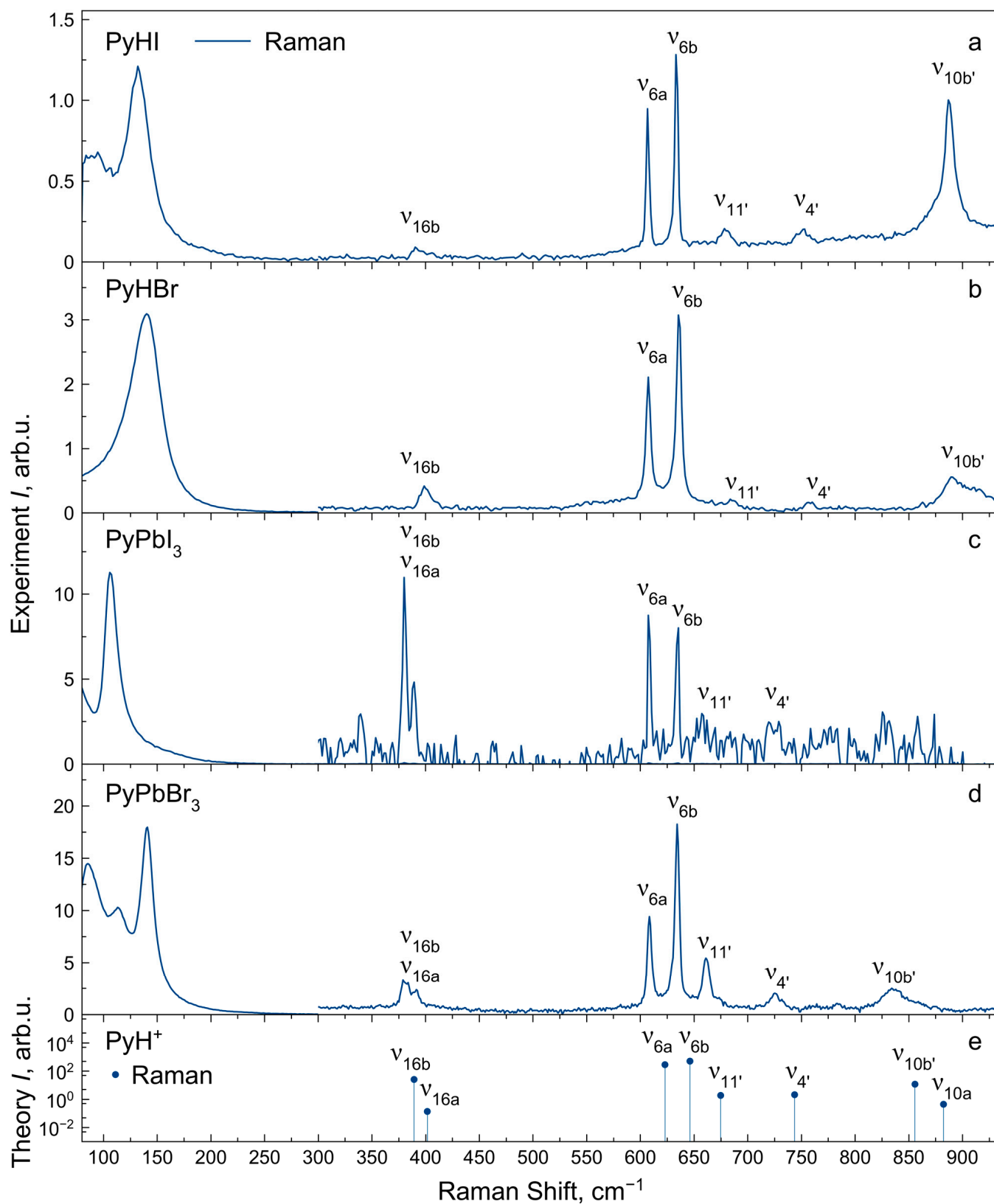


**Figure 3.** Raman spectra of PyHX salts (a,b) and PyPbX<sub>3</sub> perovskites (X<sup>−</sup> = I<sup>−</sup>, Br<sup>−</sup>) (c,d) at T = 300 K in the low-frequency region. (e) Calculated Raman intensities of PyH<sup>+</sup> cation modes.

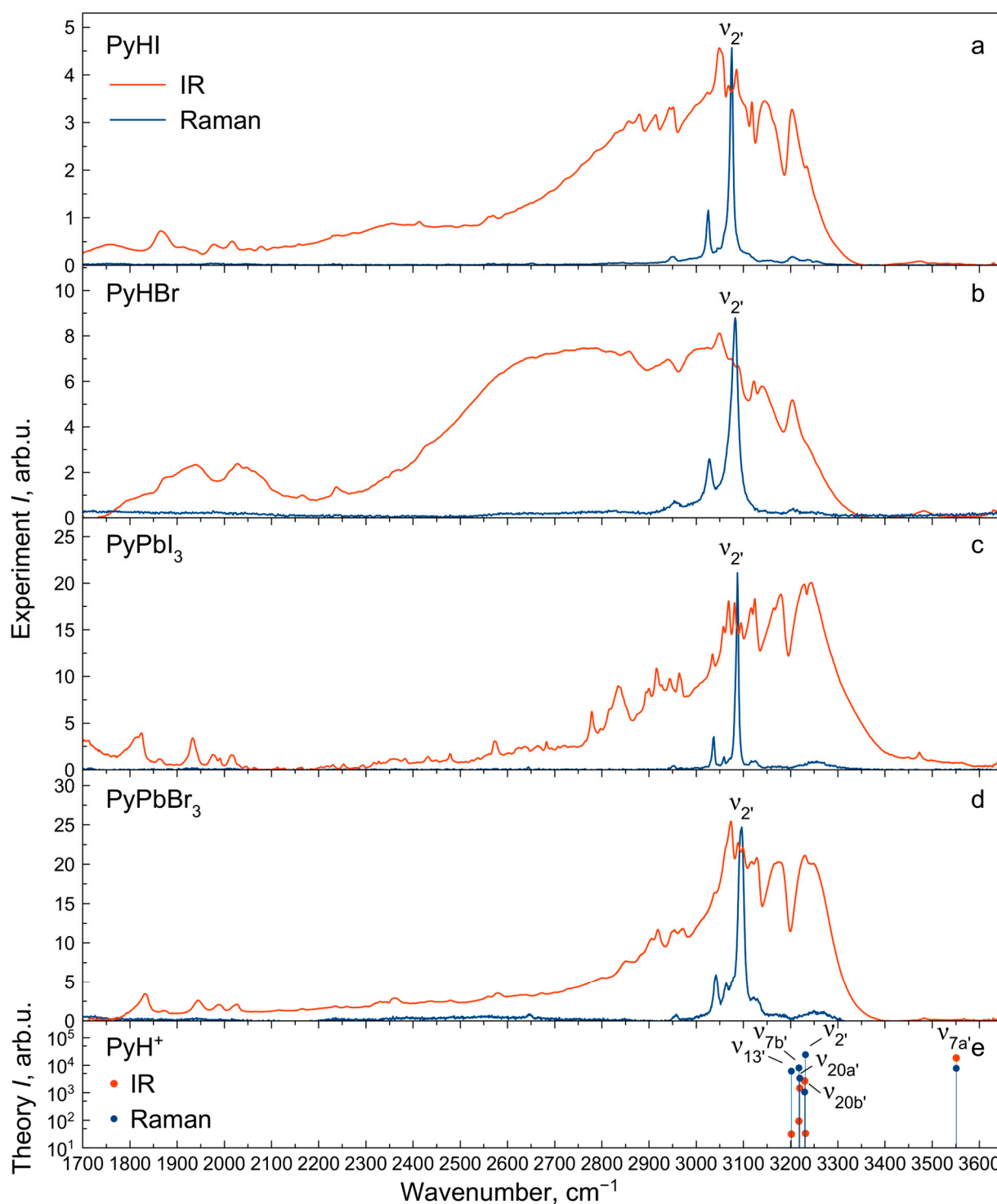


**Figure 4.** IR and Raman spectra of PyHX salts (a,b) and PyPbX<sub>3</sub> perovskites (X<sup>-</sup> = I<sup>-</sup>, Br<sup>-</sup>) (c,d) at T = 300 K in the high-frequency region. (e) Calculated IR (red) and Raman (blue) intensities of PyH<sup>+</sup> cation modes.

Three vibration modes ( $\nu_{16a}$ ,  $\nu_{10a}$ , and  $\nu_{17a}$ ) have the A<sub>2</sub> symmetry. The vibrations of this symmetry are forbidden in IR spectra. Calculations also showed that the Raman intensity of these modes is negligible. Therefore, these bands were not identified in the spectra. The intensities of unidentified vibrations in the experimental spectra are marked with the symbol “0” in Table 1.

### 2.5. Vibrational Spectra in Medium-Frequency Region

Let us consider the medium-frequency region 930–1700  $\text{cm}^{-1}$  (Figure 2). The fully symmetric  $A_1$  vibrational modes  $\nu_1$ ,  $\nu_{12}$ ,  $\nu_{8a}$ ,  $\nu_{18a}$  and  $\nu_{9a}$  are clearly recognized in all IR and Raman spectra with approximately the same frequencies in different compounds, which indicate that they are insensitive to the crystalline environment.

The doubly degenerate benzene mode  $\nu_{19}$  splits into  $\nu_{19a}$  and  $\nu_{19b}$  modes of different symmetry in the pyridinium cation. The calculated splitting of these modes is 3.5  $\text{cm}^{-1}$ . This is quite consistent with the broad unresolved band observed in salts around 1050  $\text{cm}^{-1}$ . However, in perovskites, the crystal field causes a more significant splitting of these modes for around 7  $\text{cm}^{-1}$  so that they could be potentially resolved in the IR spectra.

The vibrations  $\nu_{8b}$ ,  $\nu_{18b}$ ,  $\nu_{9b}$  (mainly consisting of stretching  $\nu_{\text{CN}}$  and in-plane bending  $\delta_{\text{NH}}$  modes) and  $\nu_{19b}$ ,  $\nu_{14}$ ,  $\nu_{15}$ ,  $\nu_3$  (mainly consisting of stretching  $\nu_{\text{CC}}$  and in-plane bending  $\delta_{\text{CH}}$  modes) have the  $B_2$  symmetry. Except for the  $\nu_{19b}$  vibration, all of them have the same frequency in the vibrational spectra of both perovskites and salts.

In the medium-frequency region, several overtones and combination modes of intense low-frequency vibrations are also observed. In order to identify these modes, the wavenumbers and intensities of normal modes and their combinations were refined by modeling in the anharmonic approximation (Table S4). The combination modes found in the spectra are summarized in Table S5 and marked by an asterisk in Figure 2.

For most of the modes with the  $A_1$  and  $B_2$  symmetries in this frequency range, no significant differences in position are observed for perovskites and salts. The  $\nu_{5'}$  and  $\nu_{17b'}$  vibrations (out-of-plane bending  $\gamma_{\text{NH}}$  and  $\gamma_{\text{CH}}$  modes, respectively) have  $B_1$  symmetry and low intensities in Raman spectra. The  $\nu_{5'}$  vibrational band fully overlaps with other bands in the 1000–1050  $\text{cm}^{-1}$  region of the IR spectra of salts. Narrower vibrational bands in the IR spectra of perovskites make it possible to assign the band at 1016  $\text{cm}^{-1}$  to the  $\nu_{5'}$  mode. In contrast, the frequency position of the  $\nu_{17b'}$  vibration is clearly defined in the IR spectra. It significantly lowers its frequency for perovskites compared to salts (from 993 to 969  $\text{cm}^{-1}$ ) and changes its shape. For PyHX ( $X^- = \text{I}^-$ ,  $\text{Br}^-$ ) salts, it has been noticed that there is a connection between the behavior of the vibrational band at 993  $\text{cm}^{-1}$  and stretching  $\nu_{\text{NH}}$  mode with the strength of the hydrogen bond [54]. The  $\nu_{17b'}$  vibration frequency is lower in perovskites as a manifestation of hydrogen bond weakening in comparison to salts.

### 2.6. Vibrational Spectra in Low-Frequency Region

For the low-frequency region of 80–950  $\text{cm}^{-1}$ , only the Raman spectra were recorded (Figure 3). Experimental IR intensities of the vibrational bands in this region are marked with the symbol “-” in Table 1. The  $\nu_{10b'}$ ,  $\nu_{4'}$  and  $\nu_{11'}$  vibrations with  $B_1$  symmetry in this region involve the  $\gamma_{\text{NH}}$  mode and lower the frequency in perovskites compared to salts. Accurate determination of the positions of these modes is important because they have high IR activity, which will lead to the appearance of overtones and combination modes in the spectrum. Measuring these modes with basic IR spectroscopy instruments is not possible. However, they are observed as weak lines in Raman spectra. Measured frequencies were used to determine spectral positions of overtones and combination frequencies in the spectrum.

The  $\nu_{6b}$  (in-plane bending  $\delta_{\text{CC}}$  mode) and  $\nu_{6a}$  (out-of-plane bending  $\gamma_{\text{CC}}$  and  $\gamma_{\text{CN}}$  modes) can be clearly assigned in Raman spectra, and its wavenumbers are almost the same for salts and perovskites. The wavenumbers of  $\nu_{16b}$  vibrations (out-of-plane bending  $\gamma_{\text{CC}}$  and  $\gamma_{\text{CN}}$  modes) can also be estimated for all compounds in Raman spectra, but the manifestation of  $\nu_{16a}$  vibrations (in-plane bending  $\delta_{\text{CC}}$  and  $\delta_{\text{CN}}$  modes) in spectra of perovskites is uncertain.

The low-frequency intense band at 135  $\text{cm}^{-1}$  in Raman spectra of halide salts is known as the rotational mode and does not depend on halide anion or hydrogen bond strength [56]. In perovskites, vibrations below 200  $\text{cm}^{-1}$  correspond to the motion of the lead halide network. Its frequencies show dependency on halide atom substitution and are lower in  $\text{PyPbI}_3$  compared to  $\text{PyPbBr}_3$ .

### 2.7. Vibrational Spectra in High-Frequency Region

The vibrational structure of the IR spectrum of halide salts and perovskites in the region of 1700–3400  $\text{cm}^{-1}$  (Figure 4) is complex. Therefore, there is no accurate assumption of the stretching vibration frequency positions, which is marked with the symbol “?” in Table 1. The exceptions are the strongest vibrational band at 3075–3096  $\text{cm}^{-1}$  in the Raman spectra ( $\nu_{2'}$  mode) and the broadest vibrational band at 1700–3300  $\text{cm}^{-1}$  in the IR spectra ( $\nu_{7a'}$  mode).

The complexity of the IR spectrum of halide salts is explained by Fermi resonances of the stretching  $\nu_{\text{NH}}$  mode ( $\nu_{7a'}$ ) with overtones and combinations of  $\text{PyH}^+$  internal modes [56–58]. An increase in the frequency and a decrease in the intensity of the  $\nu_{7a'}$  vibrational structure in the IR spectra indicates a significant hydrogen bond weakening in perovskites compared to salts. This trend and less intense and narrower Fermi resonances at the same frequencies also reveal a slight hydrogen bond weakening in  $\text{PyPbI}_3$  perovskite compared to  $\text{PyPbBr}_3$ . The low-frequency component of the  $\nu_{7a'}$  vibrational structure at 1700–2100  $\text{cm}^{-1}$  (so-called “C-band”) [58] for  $\text{PyPbBr}_3$  perovskite is slightly shifted to the higher frequencies compared to  $\text{PyPbI}_3$ , which is a manifestation of the higher vibrational coupling of the  $\nu_{\text{NH}}$  mode with other modes in this spectral region. The bands at 1800–1880  $\text{cm}^{-1}$ , 1920–1990  $\text{cm}^{-1}$  and 2010–2030  $\text{cm}^{-1}$  are formed by the stretching  $\nu_{\text{NH}}$  mode coupling with  $2\nu_{10b'}$ ,  $2\nu_{17b'}$  and  $2\nu_1$  modes, respectively. The higher frequency bands at 2880–3400  $\text{cm}^{-1}$  are formed by the  $\nu_{\text{NH}}$  mode coupling with  $2\nu_{18a}$ ,  $2\nu_{18b}$ ,  $2\nu_{9b}$ ,  $2\nu_{9a}$  modes and combinations of the last ones with lower modes.

For all IR and Raman spectra, narrower vibrational bands in the spectra of perovskites are observed compared to salts, which is due to the less disorder in perovskites. It can also be emphasized that most internal vibrational modes are not sensitive to the crystal structure (salt or perovskite) and halide anion (iodide or bromide). The exceptions are vibrational bands containing out-of-plane bending  $\gamma_{\text{NH}}$  ( $\nu_{11'}$ ,  $\nu_{4'}$ ,  $\nu_{10b'}$ ,  $\nu_{17b'}$ ,  $\nu_{5'}$ ) and stretching  $\nu_{\text{NH}}$  modes ( $\nu_{7a'}$ ), which are shown to be strongly affected by the environment [48–51,54,55]. Thus, the observation of these modes can provide information about the crystal structure of the material.

### 2.8. Vibration Splitting Effect

The intriguing feature of  $\text{PyPbX}_3$  ( $\text{X}^- = \text{I}^-, \text{Br}^-$ ) vibrational spectra is the splitting of the  $\nu_{8a}$ ,  $\nu_{8b}$ ,  $\nu_{18a}$ ,  $\nu_{18b}$ ,  $\nu_{9b}$ ,  $\nu_{9a}$  vibrational bands containing the in-plane  $\delta_{\text{NH}}$  mode (Figure 5). Such an effect can originate from one of several sources: (i) intermolecular coupling of vibrations of molecules in equivalent positions in the unit cell at  $Z > 1$  (Davydov splitting); (ii) the existence of two crystallographically non-identical cation positions in the unit cell (crystal cite effect); and (iii) the switching of cations between non-equivalent positions, leading to the splitting of involved vibrational modes.

The large interaction distance in the perovskite crystal structure speaks against the Davydov splitting effect. Splitting of the abovementioned bands was observed in the vibrational spectra of pyridinium salts of tungstophosphoric acid [59,60]. A possible explanation for this phenomenon is the mechanism of quantum tunneling of the cation between two positions, leading to the splitting of vibrations containing the NH-group bending mode. Possible mechanisms to explain the splitting observed in perovskites are the switching of pyridinium cation between non-equivalent positions and the presence of two nonequivalent crystal sites of pyridinium cations. Determining the specific nature of these splittings is possible by combining XRD and IR studies at lower temperatures. In hybrid organic–inorganic perovskites, at temperatures below room temperature, order–disorder phase transitions could be observed, caused by the “freezing out” of the movement of organic cations in the lattice. The corresponding change in the symmetry could be found from XRD data. A related issue is the presence of a pseudo two-fold axis passing through the center of C–N bond in the pyridinium cation in perovskite crystals at room temperature, which is a manifestation of the frustrated rotation of the cation between two symmetry equivalent positions.

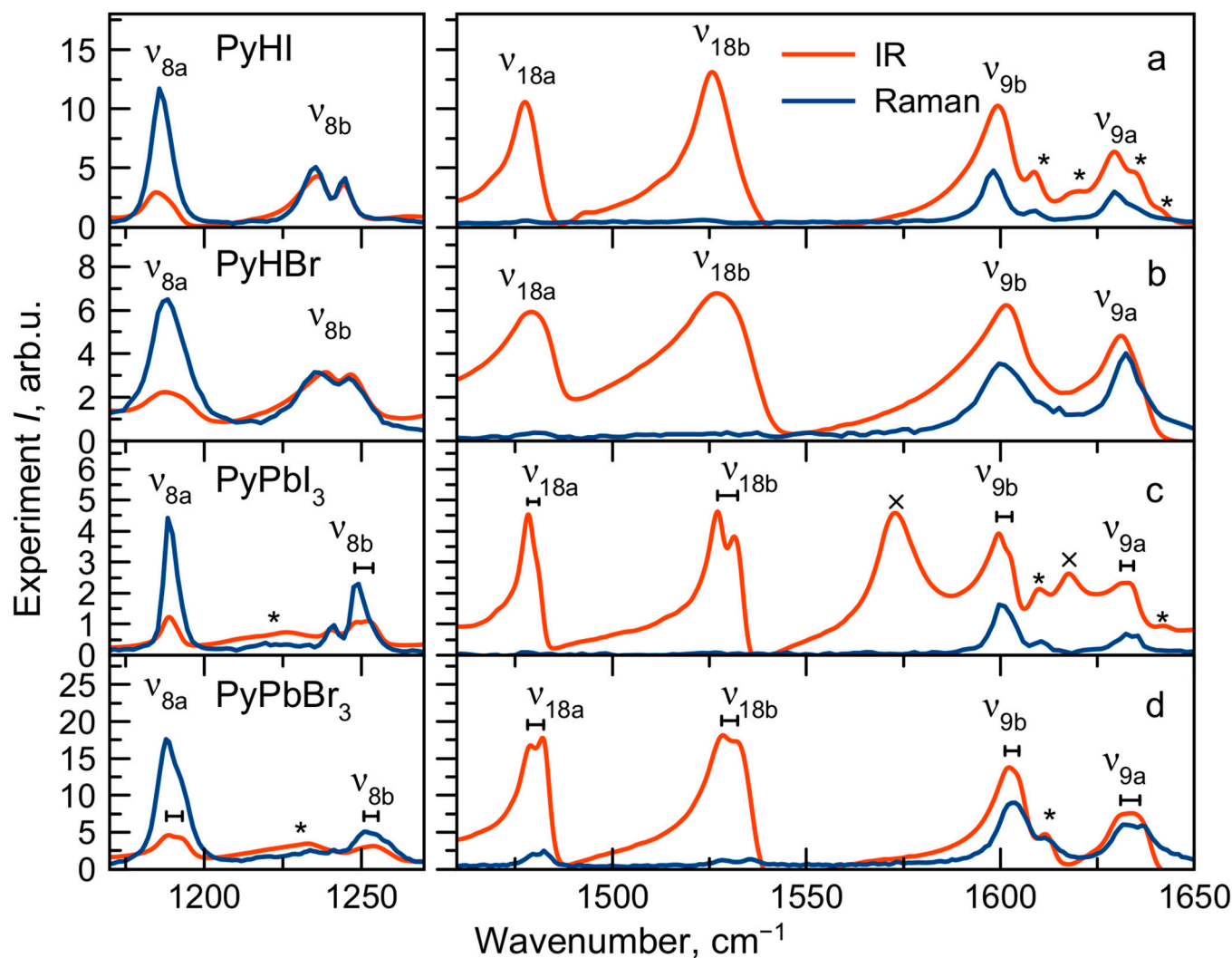


**Figure 5.** IR and Raman spectra of PyHX salts (a,b) and PyPbX<sub>3</sub> perovskites (X<sup>−</sup> = I<sup>−</sup>, Br<sup>−</sup>) (c,d) at T = 300 K in the region of split bands. \*—combination modes; ×—KI contamination bands (observed also in KI powder).

### 2.9. Solid-State NMR Study

The <sup>1</sup>H, <sup>13</sup>C and <sup>207</sup>Pb NMR spectra of PyPbX<sub>3</sub> (X<sup>−</sup> = I<sup>−</sup>, Br<sup>−</sup>) with the assignment of the signals are shown in Figure 6. There seems to be no significant difference in the state of the pyridinium cation in bromine- and iodine-based perovskite samples, except for a somewhat larger line width in the case of bromine-based perovskite, which is probably due to a larger number of structural defects in the crystalline sample. Nevertheless, in both cases, the spectra are reasonably well resolved, and only one set of relatively narrow <sup>1</sup>H and <sup>13</sup>C NMR signals is observed. The chemical shifts of <sup>207</sup>Pb NMR signals are noticeably different from those of 3D perovskites. We speculate that the values around −200 ÷ −300 ppm for PyPbBr<sub>3</sub> and around 900–1000 ppm for PyPbI<sub>3</sub> could be indicative for the formation of 1D chains of lead-halide octahedra.

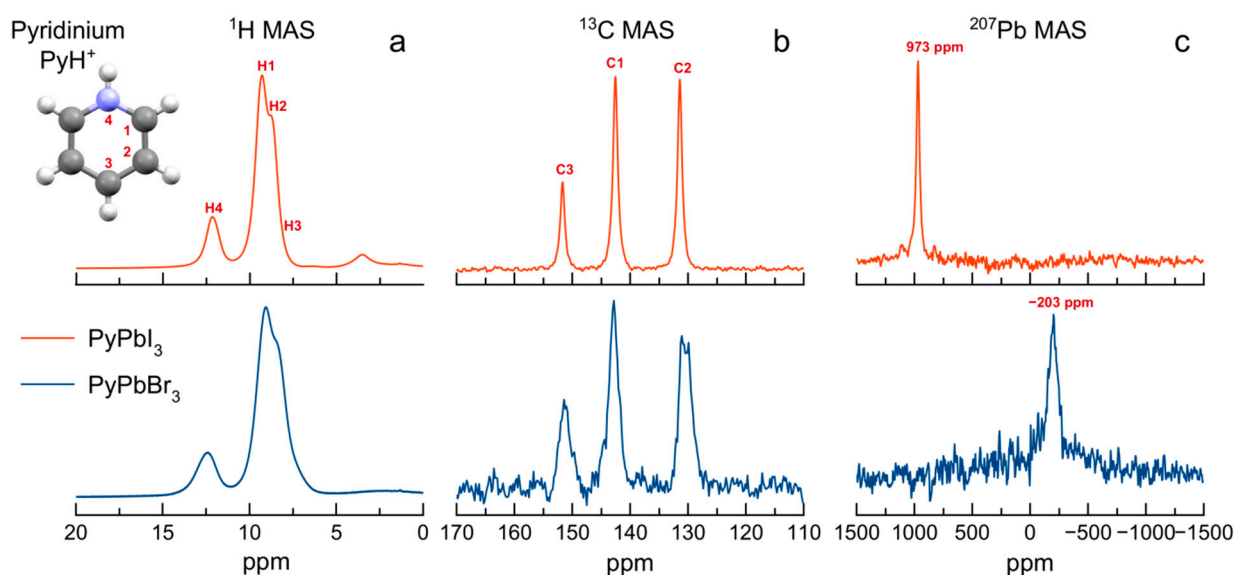


**Figure 6.** The  $^1\text{H}$  (one-pulse) (a),  $^{13}\text{C}$  (CP) (b) and  $^{207}\text{Pb}$  (Hahn-echo) (c) MAS (12.5 kHz) NMR spectra of  $\text{PyPbI}_3$  (red) and  $\text{PyPbBr}_3$  (blue) recorded at  $T = 298$  K.

### 3. Methods

**Synthesis.** Pyridinium lead trihalide  $\text{PyPbX}_3$  ( $X^- = \text{I}^-, \text{Br}^-$ ) single crystals were grown by the slow counterdiffusion of ions from individual solutions of lead(II) halides and pyridine in hydrohalic acid with 1 M concentrations in the silica gel filled U-tube. This counterdiffusion-in-gel crystallization (CGC) method could be used for synthesis of high quality hybrid organic–inorganic low-dimensional perovskites and 3D perovskites [61]. XRD data are presented in the Supplementary Materials (Figure S4). Pyridine hydrohalides  $\text{PyHX}$  ( $X^- = \text{I}^-, \text{Br}^-$ ) were synthesized by adding concentrated hydrogen halogenides drop-wise with constant stirring to the solutions of 5 mL of ethanol and 1 mL of pyridine. The resulting solutions were kept at a temperature of 3–5 °C for 12 h, then filtrated and rinsed with ethanol and dried. More details on the  $\text{PyHX}$  synthesis could be found in Selivanov et al. [31].

**DFT Calculations.** IR and Raman spectra for the  $\text{PyH}^+$  cation and  $\text{C}_6\text{H}_6$  molecule were simulated in the harmonic approximation using the Gaussian 16 software package. The wavenumbers and IR intensities of normal and combination modes were refined in the anharmonic approximation for  $\text{PyH}^+$  cation. For all calculations, the B3LYP functional and 6-311+G(d,p) basis set with one set of polarizing functions for heavy atoms (d-type) and hydrogen (p-type) were used.

**Raman Measurements.** The experimental unpolarized Raman spectra of  $\text{PyHX}$  and  $\text{PyPbX}_3$  ( $X^- = \text{I}^-, \text{Br}^-$ ) were acquired at  $T = 300$  K using the Horiba Jobin-Yvon LabRam HR800 confocal Raman spectrometer (Horiba Jobin-Yvon, Oberursel, Germany) in backscattering geometry (see Figure S5 for the scheme of the Raman measurements). The equipment used a diffraction grating with a cell of 1800 L/mm and the aperture was  $150 \times 150 \mu\text{m}$ . Laser radiation was focused through a  $100\times$  objective lens. A solid-state laser with a wavelength of 532 nm was utilized as the radiation source. The actual laser power applied to the sample was around 6 mW, with 10 s of accumulation time and 6 repetitions.

**IR Measurements.**  $\text{PyHX}$  and  $\text{PyPbX}_3$  crystals were subjected to grinding in a mortar and mixed with KX powders (where  $X^- = \text{I}^-, \text{Br}^-$ ) in a weight ratio of 1:10 for I and 1:3 for Br, respectively. IR absorption spectra were recorded in the  $850\text{--}4000 \text{ cm}^{-1}$  spectral range with a spectral resolution of  $2 \text{ cm}^{-1}$  applying the Happ–Gensel apodization using a research-grade FT-IR spectrometer Thermo Nicolet iS50 (Thermo Scientific, Waltham, MA, USA). Spectrometer was equipped with a DTGS detector and a KBr beamsplitter.

**Solid-state NMR Measurements.** The  $^1\text{H}$ ,  $^{13}\text{C}$  and  $^{207}\text{Pb}$  NMR measurements were performed using Bruker Avance III 400WB NMR spectrometers (Bruker, Ettlingen, Germany)

(working frequency 400.23 MHz for  $^1\text{H}$ , 100.65 MHz for  $^{13}\text{C}$  and 83.73 MHz for  $^{207}\text{Pb}$ ). The spectra were recorded under magic angle spinning conditions (MAS; spinning rate 12 kHz) at room temperature using 4.0 mm rotor.  $^{13}\text{C}$  MAS NMR spectra were measured using cross-polarization (CP) technique (2 ms contact time);  $^{207}\text{Pb}$  NMR spectra were measured using Hahn echo technique. The relaxation delays were set to 120 s for  $^1\text{H}$ , 2–5 s for  $^{13}\text{C}$  and 1 s for  $^{207}\text{Pb}$ . Liquid TMS at 0 ppm was used as an external reference for  $^1\text{H}$  and  $^{13}\text{C}$  spectra.  $\text{Pb}(\text{NO}_3)_2$  at  $-3482$  ppm (under 4 kHz spinning with  $25^\circ\text{C}$  room temperature) was used as an external reference for  $^{207}\text{Pb}$  spectra.

#### 4. Conclusions

We conducted a study of the internal vibrations of the pyridinium cation  $\text{PyH}^+$  in four materials:  $\text{PyHX}$  salts and  $\text{PyPbX}_3$  ( $\text{X}^- = \text{I}^-, \text{Br}^-$ ) 1D-perovskites. The bands experimentally observed in the Raman scattering and IR absorption spectra were identified by analyzing the symmetry of vibrations and comparing them with the results of DFT calculations for a free benzene molecule and a pyridinium cation. Most internal vibrations of  $\text{PyH}^+$  are not significantly influenced by the crystalline environment. However, vibrational modes  $\nu_{11'}$ ,  $\nu_{4'}$ ,  $\nu_{10b'}$ ,  $\nu_{17b'}$ ,  $\nu_{5'}$  and  $\nu_{7a'}$  undergo strong shifts upon the transition from salts to perovskites. What these modes have in common is the presence of NH-group movements in them, which, apparently, are influenced by the environment, in particular, by the changes in the strength of the hydrogen bond. In perovskites, splitting of non-degenerate modes  $\nu_{8a}$ ,  $\nu_{8b}$ ,  $\nu_{18a}$ ,  $\nu_{18b}$ ,  $\nu_{9b}$ ,  $\nu_{9a}$  is observed. This phenomenon can be explained by different mechanisms, which could be distinguished by a joint XRD and IR study at lower temperatures. This work illustrates the different crystalline environment influence on organic cations behavior such as vibrational band shifts, changes in their intensities and width and splitting of non-degenerate levels. In this way, organic cations act as spectators, probes of the crystalline environment in hybrid organic–inorganic crystals, including halide perovskites, and provide valuable information on the dynamics of the system. Thus, spectroscopy of internal vibrations of organic cations can be a convenient and informative tool for studying these new materials towards new photonics applications.

**Supplementary Materials:** The following supporting information can be downloaded at: <https://www.mdpi.com/article/10.3390/molecules29010078/s1>, Figure S1: Photos of  $\text{PyPbI}_3$  (a) and  $\text{PyPbBr}_3$  (b) single crystals; Table S1: Character table of  $D_{6h}$  point symmetry group; Figure S2: Transformation of  $\text{C}_6\text{H}_6$  to  $\text{PyH}^+$  by symmetry elements; Table S2: Character table of  $C_{2v}$  point symmetry group; Table S3: Correspondence between the irreducible representations of the  $D_{6h}$  and  $C_{2v}$  point symmetry groups; Figure S3: Calculated atomic displacements in internal normal modes of the  $\text{PyH}^+$  cation. The notation in Wilson nomenclature and symmetry of the modes are labeled. Red crosses and dots indicate out-of-plane atomic displacements; Table S4: Calculated anharmonic fundamental modes (from 1 to 30), overtones (Over) and combination modes (Comb) of the  $\text{PyH}^+$  cation; Table S5: Combination modes recognized in the experimental vibrational spectra; Figure S4: Powder XRD patterns simulated from the single crystal data (a,c) and measured for grounded single crystals (b,d) for  $\text{PyPbI}_3$  (a,b) and  $\text{PyPbBr}_3$  (c,d); Figure S5: The scheme of the Raman measurement experiment.

**Author Contributions:** Conceptualization, Y.V.K.; Investigation, A.Y.S., A.Y.M., K.M.B., N.I.S., A.S.M., P.M.T. and Y.V.K.; Writing—original draft, A.Y.S.; Writing—review & editing, A.Y.S., C.C.S. and Y.V.K.; Visualization, A.Y.S.; Supervision, Y.V.K. All authors have read and agreed to the published version of the manuscript.

**Funding:** This research has been supported by the Ministry of Science and Higher Education of the Russian Federation (Megagrant no. 075-15-2022-1112).

**Institutional Review Board Statement:** Not applicable.

**Informed Consent Statement:** Not applicable.

**Data Availability Statement:** Data are contained within the article and Supplementary Materials.

**Acknowledgments:** This work was carried out on the equipment of the SPbU Research Centers “Nanophotonics”, “Center for Optical and Laser materials research”, “X-ray Diffraction Studies”,

“Geomodel”, “Magnetic Resonance Research Centre”, “Centre for Diagnostics of Functional Materials for Medicine, Pharmacology and Nanoelectronics”, “Thermogravimetric and Calorimetric Research Centre”, “Computer Center of SPbU” (<http://cc.spbu.ru>, accessed on 19 December 2023) and research facilities of the laboratory “Photoactive Nanocomposite Materials” (SPbU ID: 91696387).

**Conflicts of Interest:** The authors declare no conflict of interest.

## References

1. Yang, C.; Yin, J.; Li, H.; Almasabi, K.; Gutiérrez-Arzaluz, L.; Gereige, I.; Brédas, J.-L.; Bakr, O.M.; Mohammed, O.F. Engineering Surface Orientations for Efficient and Stable Hybrid Perovskite Single-Crystal Solar Cells. *ACS Energy Lett.* **2022**, *7*, 1544–1552. [CrossRef]
2. Pang, P.; Jin, G.; Liang, C.; Wang, B.; Xiang, W.; Zhang, D.; Xu, J.; Hong, W.; Xiao, Z.; Wang, L.; et al. Rearranging Low-Dimensional Phase Distribution of Quasi-2D Perovskites for Efficient Sky-Blue Perovskite Light-Emitting Diodes. *ACS Nano* **2020**, *14*, 11420–11430. [CrossRef] [PubMed]
3. Qin, C.; Sandanayaka, A.S.D.; Zhao, C.; Matsushima, T.; Zhang, D.; Fujihara, T.; Adachi, C. Stable Room-Temperature Continuous-Wave Lasing in Quasi-2D Perovskite Films. *Nature* **2020**, *585*, 53–57. [CrossRef] [PubMed]
4. Furlan, F.; Nodari, D.; Palladino, E.; Angela, E.; Mohan, L.; Briscoe, J.; Fuchter, M.J.; Macdonald, T.J.; Grancini, G.; McLachlan, M.A.; et al. Tuning Halide Composition Allows Low Dark Current Perovskite Photodetectors With High Specific Detectivity. *Adv. Opt. Mater.* **2022**, *10*, 2201816. [CrossRef]
5. Selivanov, N.I.; Samsonova, A.Y.; Kevorkyants, R.; Krauklis, I.V.; Chizhov, Y.V.; Stroganov, B.V.; Triantafyllou-Rundell, M.E.; Bahnemann, D.W.; Stoumpos, C.C.; Emeline, A.V.; et al. Hybrid Organic–Inorganic Halide Post-Perovskite 3-Cyanopyridinium Lead Tribromide for Optoelectronic Applications. *Adv. Funct. Mater.* **2021**, *31*, 2102338. [CrossRef]
6. Jung, M.-H. Diammonium spacer-induced stable zigzag type 2D Dion–Jacobson lead/tin-based perovskite solar cells. *Dalton Trans.* **2023**, *52*, 17258–17272. [CrossRef]
7. Biswas, A.; Bakthavatsalam, R.; Shaikh, S.R.; Shinde, A.; Lohar, A.; Jena, S.; Gonnade, R.G.; Kundu, J. Efficient Broad-Band Emission from Contorted Purely Corner-Shared One Dimensional (1D) Organic Lead Halide Perovskite. *Chem. Mater.* **2019**, *31*, 2253–2257. [CrossRef]
8. Qi, Z.; Gao, H.; Yang, X.; Chen, Y.; Zhang, F.-Q.; Qu, M.; Li, S.-L.; Zhang, X.-M. A One-Dimensional Broadband Emissive Hybrid Lead Iodide with Face-Sharing PbI<sub>6</sub> Octahedral Chains. *Inorg. Chem.* **2021**, *60*, 15136–15140. [CrossRef]
9. Whitfield, P.; Herron, N.; Guise, W.; Page, K.; Cheng, Y.Q.; Milas, I.; Crawford, M.K. Structures, Phase Transitions and Tricritical Behavior of the Hybrid Perovskite Methyl Ammonium Lead Iodide. *Sci. Rep.* **2016**, *6*, 35685. [CrossRef]
10. Driscoll, E.H.; Orera, A.; Anderson, P.A.; Sanjuán, M.L.; Slater, P.R. Raman Spectroscopy Insights into the  $\alpha$ - and  $\delta$ -Phases of Formamidinium Lead Iodide (FAPbI<sub>3</sub>). *Dalton Trans.* **2021**, *50*, 3315. [CrossRef]
11. Maćzka, M.; Ptak, M. Temperature-Dependent Raman Studies of FAPbBr<sub>3</sub> and MAPbBr<sub>3</sub> Perovskites: Effect of Phase Transitions on Molecular Dynamics and Lattice Distortion. *Solids* **2022**, *3*, 111–121. [CrossRef]
12. Ghosh, S.; Rana, D.; Pradhan, B.; Donfack, P.; Hofkens, J.; Materny, A. Raman Spectroscopy of Formamidinium-Based Lead Mixed-Halide Perovskite Bulk Crystals. *ChemPhysChem* **2023**, *24*, e202300303. [CrossRef]
13. Naqvi, F.H.; Junaid, S.B.; Ko, J.-H. Influence of Halides on Elastic and Vibrational Properties of Mixed-Halide Perovskite Systems Studied by Brillouin and Raman Scattering. *Materials* **2023**, *16*, 3986. [CrossRef] [PubMed]
14. Lavén, R.; Koza, M.M.; Malavasi, L.; Perrichon, A.; Appel, M.; Karlsson, M. Rotational Dynamics of Organic Cations in Formamidinium Lead Iodide Perovskites. *J. Phys. Chem. Lett.* **2023**, *14*, 2784–2791. [CrossRef]
15. Brown, K.L.; Parker, S.F.; García, I.R.; Mukhopadhyay, S.; Sakai, V.G.; Stock, C. Molecular Orientational Melting within a Lead-Halide Octahedron Framework: The Order-Disorder Transition in CH<sub>3</sub>NH<sub>3</sub>PbBr<sub>3</sub>. *Phys. Rev. B* **2017**, *96*, 174111. [CrossRef]
16. Schuck, G.; Lehmann, F.; Ollivier, J.; Mutka, H.; Schorr, S. Influence of Chloride Substitution on the Rotational Dynamics of Methylammonium in MAPbI<sub>3-x</sub>Cl<sub>x</sub> Perovskites. *J. Phys. Chem. C* **2019**, *123*, 11436–11446. [CrossRef]
17. Chen, T.; Foley, B.J.; Ipek, B.; Tyagi, M.; Copley, J.R.D.; Brown, C.M.; Choi, J.J.; Lee, S.-H. Rotational Dynamics of Organic Cations in the CH<sub>3</sub>NH<sub>3</sub>PbI<sub>3</sub> Perovskite. *Phys. Chem. Chem. Phys.* **2015**, *17*, 31278–31286. [CrossRef]
18. Even, J.; Carignano, M.; Katan, C. Molecular disorder and translation/rotation coupling in the plastic crystal phase of hybrid perovskites. *Nanoscale* **2016**, *8*, 6222–6236. [CrossRef] [PubMed]
19. Cui, Y.; Liu, Y.-Y.; Deng, J.-P.; Zhang, X.-Z.; Yang, R.-B.; Li, Z.-Q.; Wang, Z.-W. Microscopic theory of Raman scattering for the rotational organic cation in metal halide perovskites. *Phys. Rev. B* **2023**, *107*, 094306. [CrossRef]
20. Kim, Y.; Bae, S.; Park, J.; Nguyen, T.T.T.; Jung, H.R.; Jo, W.; Kim, Y.-H.; Raebiger, H.; Yoon, S. Parallel Alignment of Methylammonium Cations in an Orthorhombic CH<sub>3</sub>NH<sub>3</sub>PbCl<sub>3</sub> Single Crystal Observed by Polarized Micro-Raman Scattering Spectroscopy. *Chem. Mater.* **2022**, *34*, 2972–2980. [CrossRef]
21. Menahem, M.; Dai, Z.; Aharon, S.; Sharma, R.; Asher, M.; Diskin-Posner, Y.; Korobko, R.; Rappe, A.M.; Yaffe, O. Strongly Anharmonic Octahedral Tilting in Two-Dimensional Hybrid Halide Perovskites. *ACS Nano* **2021**, *15*, 10153–10162. [CrossRef] [PubMed]

22. Lavan, S.N.; Sanni, A.M.; Rury, A.S.; Liu, Z.-F. Characterization of the Ammonium Bending Vibrations in Two-Dimensional Hybrid Lead-Halide Perovskites from Raman Spectroscopy and First-Principles Calculations. *J. Phys. Chem. C* **2021**, *125*, 223–236. [[CrossRef](#)]
23. Dhanabalan, B.; Leng, Y.-C.; Biffi, G.; Lin, M.-L.; Tan, P.-H.; Infante, I.; Manna, L.; Arciniegas, M.P.; Krahne, R. Directional Anisotropy of the Vibrational Modes in 2D-Layered Perovskites. *ACS Nano* **2020**, *14*, 4689–4697. [[CrossRef](#)] [[PubMed](#)]
24. Fedoruk, K.; Drozdowski, D.; Maczka, M.; Zareba, J.K.; Stefańska, D.; Gagor, A.; Sieradzki, A. [Methylhydrazinium]<sub>2</sub>PbCl<sub>4</sub>, a Two-Dimensional Perovskite with Polar and Modulated Phases. *Inorg. Chem.* **2022**, *61*, 15520–15531. [[CrossRef](#)] [[PubMed](#)]
25. Li, H.-J.; Liu, Y.-L.; Chen, X.-G.; Gao, J.-X.; Wang, Z.-X.; Liao, W.-Q. High-Temperature Dielectric Switching and Photoluminescence in a Corrugated Lead Bromide Layer Hybrid Perovskite Semiconductor. *Inorg. Chem.* **2019**, *58*, 10357–10363. [[CrossRef](#)] [[PubMed](#)]
26. Tao, K.; Han, S.; Ji, C.; Liu, X.; Wu, Z.; Zhang, J.; Luo, J.; Sun, Z. Structural Phase Transition and Switchable Dielectric Properties of a Unique Two-Dimensional Organic–Inorganic Hybrid Perovskite Compound [C<sub>6</sub>H<sub>11</sub>NH<sub>2</sub>CH<sub>3</sub>]<sub>4</sub>Pb<sub>3</sub>I<sub>10</sub>. *Cryst. Growth Des.* **2018**, *18*, 7316–7322. [[CrossRef](#)]
27. Zeb, A.; Sun, Z.; Khan, A.; Zhang, S.; Khan, T.; Asghara, M.A.; Luo, J. [C<sub>6</sub>H<sub>14</sub>N]PbI<sub>3</sub>: A One-Dimensional Perovskite-Like Order–Disorder Phase Transition Material with Semiconducting and Switchable Dielectric Attributes. *Inorg. Chem. Front.* **2018**, *5*, 897–902. [[CrossRef](#)]
28. Peng, H.; Liu, Y.-H.; Huang, X.-Q.; Liu, Q.; Yu, Z.-H.; Wang, Z.-X.; Liao, W.-Q. Homochiral One-Dimensional ABX<sub>3</sub> Lead Halide Perovskites with High-T<sub>c</sub> Quadratic Nonlinear Optical and Dielectric Switchings. *Mater. Chem. Front.* **2021**, *5*, 4756–4763. [[CrossRef](#)]
29. Fedoruk, K.; Zelewski, S.J.; Zareba, J.K.; Ptak, M.; Maczka, M.; Sieradzki, A. Getting the Details Right: Optical, Dielectric, and Vibrational Outcomes of Structural Phase Transition in One-Dimensional Pyrrolidinium Lead Iodide and the Role of Defects. *J. Mater. Chem. C* **2022**, *10*, 10519–10529. [[CrossRef](#)]
30. Zienkiewicz, J.A.; Kałduńska, K.; Fedoruk, K.; Barros dos Santos, A.J.; Stefanski, M.; Paraguassu, W.; Muzioł, T.M.; Ptak, M. Luminescence and Dielectric Switchable Properties of a 1D (1,1,1-Trimethylhydrazinium)PbI<sub>3</sub> Hybrid Perovskitoid. *Inorg. Chem.* **2022**, *61*, 20886–20895. [[CrossRef](#)]
31. Selivanov, N.I.; Rozhkova, Y.A.; Kevorkyants, R.; Emeline, A.V.; Bahnemann, D.W. The Effect of Organic Cations on the Electronic, Optical and Luminescence Properties of 1D Piperidinium, Pyridinium, and 3-Hydroxypyridinium Lead Trihalides. *Dalton Trans.* **2020**, *49*, 4390–4403. [[CrossRef](#)] [[PubMed](#)]
32. Geselle, M.; Fuess, H. Crystal structure of pyridinium triiodoplumbate(II), C<sub>5</sub>H<sub>6</sub>NPbI<sub>3</sub>. *Z. Kristallogr. New Cryst. Struct.* **1997**, *212*, 235. [[CrossRef](#)]
33. Samsonova, A.Y.; Krauklis, I.V.; Chizhov, Y.V.; Selivanov, N.I.; Emeline, A.V.; Kapitonov, Y.V. Polarized Raman Study of Internal Vibrations of the Organic Cation in 3-Cyanopyridinium Lead Tribromide Post-perovskite. *J. Phys. Chem. Lett.* **2023**, *14*, 3445–3451. [[CrossRef](#)] [[PubMed](#)]
34. Krauklis, I.V.; Samsonova, A.Y.; Selivanov, N.I.; Kapitonov, Y.V.; Chizhov, Y.V. Cluster approach for the density functional theory study of organic cation vibrations in hybrid halide post-perovskite 3-cyanopyridinium lead tribromide. *J. Raman Spectrosc.* **2023**, *1*. [[CrossRef](#)]
35. Moral, R.F.; Germino, J.C.; Bonato, L.G.; Almeida, D.B.; Therézio, E.M.; Atvars, T.D.Z.; Stranks, S.D.; Nome, R.A.; Nogueira, A.F. Influence of the Vibrational Modes from the Organic Moieties in 2D Lead Halides on Excitonic Recombination and Phase Transition. *Adv. Opt. Mater.* **2020**, *8*, 2001431. [[CrossRef](#)]
36. Waśicki, J.; Nawrocki, W.; Pająk, Z.; Natkaniec, I.; Belushkin, A.V. Neutron Scattering Study of Some Pyridinium Salts. *Phys. Stat. Sol. A* **1989**, *114*, 497–504. [[CrossRef](#)]
37. Ripmeester, J.A. <sup>1</sup>H and <sup>2</sup>H NMR Study of Pyridinium Iodide. Disorder and Molecular Motion between Inequivalent Sites. *J. Chem. Phys.* **1986**, *85*, 747–750. [[CrossRef](#)]
38. Mukhopadhyay, R.; Mitra, S.; Tsukushi, I.; Ikeda, S. Order–Disorder Transition in Pyridinium Iodide: Quasi-Elastic Neutron Scattering Study. *Chem. Phys. Lett.* **2001**, *341*, 45–50. [[CrossRef](#)]
39. Szafranski, M.; Szafraniak, I. Phase Transitions and Pressure Effects in Simple Pyridinium Salts. *J. Phys. Condens. Matter* **2003**, *15*, 5933. [[CrossRef](#)]
40. Pajzderska, A.; Gonzalez, M.A.; Waśicki, J. Dynamics in Molecular and Molecular-Ionic Crystals: A Combined Experimental and Molecular Simulation Study of Reorientational Motions in Benzene, Pyridinium Iodide, and Pyridinium Nitrate. *J. Chem. Phys.* **2013**, *138*, 024508. [[CrossRef](#)]
41. Selivanov, N.I.; Murashkina, A.A.; Kevorkyants, R.; Emeline, A.V.; Bahnemann, D.W. Pyridinium Lead Tribromide and Pyridinium Lead Triiodide: Quasi-One-Dimensional Perovskites with an Optically Active Aromatic π-System. *Dalton Trans.* **2018**, *47*, 16313–16319. [[CrossRef](#)]
42. Yan, Z.S.; Long, J.Y.; Gong, Y. Three in situ—Synthesized novel inorganic-organic hybrid materials based on metal (M = Bi, Pb) iodide and organoamine using one-pot reactions: Structures, band gaps and optoelectronic properties. *New J. Chem.* **2018**, *42*, 699–707. [[CrossRef](#)]
43. Hartl, V.H. Die Kristallstruktur von Pyridiniumjodid. *Acta Cryst.* **1975**, *B31*, 1781. [[CrossRef](#)]
44. Pająk, Z.; Szafranska, B.; Czarnecki, P.; Mayer, J.; Kozak, A. Polymorphic Phase Transitions and Molecular Motion in Pyridinium Chlorochromate. *Chem. Phys. Lett.* **1997**, *274*, 106–111.

45. Asaji, T.; Fujimori, H.; Ishida, H.; Eda, K.; Hashimoto, M.; Oguni, M. Calorimetric and Single Crystal X-Ray Study of the Phase Transition of  $(\text{PyH})_2\text{PdCl}_4$ . *J. Phys. Chem. Solids* **2005**, *66*, 869–875. [[CrossRef](#)]
46. Waśicki, J.; Pajzderska, A.; Fojud, Z. Temperature Dependence of Spontaneous Polarization in Order–Disorder Pyridinium Periodate Extracted from  $^2\text{H}$  NMR Data. *J. Phys. Chem. C* **2008**, *112*, 7503–7508.
47. Pająk, Z.; Wolak, J.; Połomska, M. NIR Raman Study of Ferroelectric Phase Transitions in Pyridinium Tetrafluoroborate. *Ferroelectrics* **2004**, *303*, 207–210.
48. Wong, P.T.T.; Ripmeester, J.A. The Phase Transition and Reorientational Fluctuations in Pyridinium Iodide Crystal Investigated by Raman Scattering. *Chem. Phys. Lett.* **1980**, *72*, 122–126. [[CrossRef](#)]
49. Józków, J.; Jakubas, R.; Baran, J. Infrared Investigation of the Order–Disorder Phase Transitions in  $(\text{C}_5\text{H}_5\text{NH})_6\text{Bi}_4\text{Cl}_{18}$ . *J. Mol. Struct.* **2000**, *555*, 273–279. [[CrossRef](#)]
50. Tarasiewicz, J.; Jakubas, R.; Bator, G.; Zaleski, J.; Baran, J.; Medycki, W. Structural Characterization, Thermal, Dielectric, Vibrational Properties and Molecular Dynamics of  $(\text{C}_5\text{H}_5\text{NH})_3\text{BiCl}_6$ . *J. Mol. Struct.* **2009**, *932*, 6–15. [[CrossRef](#)]
51. Jesariew, D.; Ilczyszyn, M.M. Crystal Structure, Phase Transition, and Disorder in Pyridinium Methanesulfonate. *J. Phys. Chem. Solids* **2017**, *104*, 304–314. [[CrossRef](#)]
52. Groom, C.R.; Bruno, I.J.; Lightfoot, M.P.; Ward, S.C. The Cambridge Structural Database. *Acta Cryst.* **2016**, *B72*, 171–179. [[CrossRef](#)] [[PubMed](#)]
53. Wilson, E.B., Jr. The Normal Modes and Frequencies of Vibration of the Regular Plane Hexagon Model of the Benzene Molecule. *Phys. Rev.* **1934**, *45*, 706. [[CrossRef](#)]
54. Cook, D. Vibrational Spectra of Pyridinium Salts. *Can. J. Chem.* **1961**, *39*, 2009–2024. [[CrossRef](#)]
55. Gardner, A.M.; Wright, T.J. Consistent Assignment of the Vibrations of Monosubstituted Benzenes. *J. Chem. Phys.* **2011**, *135*, 114305. [[CrossRef](#)] [[PubMed](#)]
56. Foglizzo, R.; Novak, A. Low Frequency Infrared and Raman Spectra of Hydrogen Bonded Pyridinium Halides. *J. Chem. Phys.* **1969**, *50*, 5366. [[CrossRef](#)]
57. Glazunov, V.P.; Odinkov, S.E. Infrared Spectra of Pyridinium Salts in Solution-I. The Region of Middle Frequencies. *Spectrochim. Acta* **1982**, *38A*, 399–408. [[CrossRef](#)]
58. Glazunov, V.P.; Odinkov, S.E. Infrared Spectra of Pyridinium Salts in Solution-II. Fermi Resonance and Structure of  $\nu_{\text{NH}}$  Bands. *Spectrochim. Acta* **1982**, *38A*, 409–415. [[CrossRef](#)]
59. Pichon, C.; Mialane, P.; Marrot, J.; Binet, C.; Vimont, A.; Travert, A.; Lavalley, J.-C. Combined XRD and Infrared Studies of Pyridinium Species in  $(\text{PyH})_3[\text{PW}_{12}\text{O}_{40}]$  Single Crystals. *Phys. Chem. Chem. Phys.* **2011**, *13*, 322–327. [[CrossRef](#)]
60. Binet, C.; Travert, A.; Daturi, M.; Lavalley, J.-C.; Vimont, A. Unusual IR Ring Mode Splittings for Pyridinium Species in  $\text{H}_3\text{PW}_{12}\text{O}_{40}$  Heteropolyacid: Involvement of the  $\delta_{\text{NH}}$  Internal Mode. *RSC Adv.* **2014**, *4*, 19159. [[CrossRef](#)]
61. Selivanov, N.I.; Murzin, A.O.; Yudin, V.I.; Kapitonov, Y.V.; Emeline, A.V. Counterdiffusion-In-Gel Growth of High Optical and Crystal Quality  $\text{MAPbX}_3$  ( $\text{MA} = \text{CH}_3\text{NH}_3^+$ ,  $\text{X} = \text{I}^-$ ,  $\text{Br}^-$ ) Lead-Halide Perovskite Single Crystals. *CrystEngComm* **2022**, *24*, 2976–2981. [[CrossRef](#)]

**Disclaimer/Publisher’s Note:** The statements, opinions and data contained in all publications are solely those of the individual author(s) and contributor(s) and not of MDPI and/or the editor(s). MDPI and/or the editor(s) disclaim responsibility for any injury to people or property resulting from any ideas, methods, instructions or products referred to in the content.